Grevemeyer, I., et al., 2022, The continent-to-ocean transition in the Iberia Abyssal Plain: Geology, https://doi.org/10.1130/G49753.1

The continent to ocean transition in the Iberia Abyssal Plain

Ingo Grevemeyer[1], Cesar R. Ranero[2, 3], Cord Papenberg[1], Valenti Sallares[2], Rafael Bartolomé[2], Manel Prada[2], Luis Batista[4, 5], and Marta Neres[4, 5]

[1] GEOMAR Helmholtz Centre for Ocean Research, Kiel, 24148 Kiel, Germany

[2] Barcelona Center for Subsurface Imaging, Institut de Ciències del Mar, CSIC, 08003 Barcelona, Spain

[3] ICREA, 08003 Barcelona, Spain

[4] Instituto Português do Mar e da Atmosfera, 1749-077 Lisboa, Portugal

[5] Instituto Dom Luiz, University of Lisbon, 1749-016 Lisboa, Portugal

MAGNETIC FIELD OVER THE IBERIA ABYSSAL PLAIN

The location of the magnetic J-anomaly in the Iberia Abyssal Plain discussed in this manuscript (Fig. 1) is derived from gridded surface shipboard magnetic data (Verhoef et al., 1996), shown in Fig. S1. Further, along FRAME-p3, we recorded the total magnetic field using a SeaSpy marine magnetometer. Acquired data were corrected by removing the local magnitude of the internal magnetic field assuming the International Geomagnetic Reference Field model (IGRF) (Thébault et al., 2015) and the external field variation using base station data from the Observatório Geofísico e Astronómico da Universidade de Coimbra, OGAUC (https://www.uc.pt/org/observatorio/observacoes). Data are displayed in Fig. 3D and Fig. S4 are smoothed using a 1 km median filter and are displayed using Generic Mapping Tools (https://gmt.soest.hawaii.edu).

DATA ACQUISITION

During the project FRAME aboard the Spanish research vessel Sarmiento de Gamboa, thirty ocean-bottom-seismometers (OBS) and hydrophones (OBH) were deployed in September of 2018 along the 360 km long seismic profile p3 in the Iberia Abyssal Plain, recording shots

from a tuned airgun array of 4,300 cubic inches. OBS/H, deployed at a variable instrument spacing of 10 to 12 km, provided excellent P-wave data, including arrivals sampling a number of near vertical reflections and even wide-angle reflections from the top of basement as well as energy turning in the thick sedimentary cover (Ps). Examples are shown in Fig. S2a to S2d. In addition to sedimentary refraction branches most prominent are crustal arrivals (Pg) and an uppermost mantle refraction branch (Pn). Pg arrivals are interpreted to have apparent velocities of <6 km/s. Further, stations in the western domain of the profiles also recorded some wide-angle reflections from the crust-mantle boundary (PmP) as secondary arrivals. Note that PmP arrivals are absent in the eastern domain, where we observe seismic apparent velocities of ~ 8 km/s at very short offsets, revealing a shallow mantle. At stations where mantle arrivals occur at short offsets, we were not able to distinguish between the Pg and Pn (see Fig. S3a-S3d). Data used in this study are archived at https://www.pangaea.de.

MIRROR IMAGING

Unfortunately, along FRAME-p3 no multi-channel seismic reflection data are available. However, OBH/S records provide excellent recordings of the near-vertical reflections in the first water-layer-multiple, carrying information of the sedimentary column. We therefore used a technique called “mirror imaging and migration” (Grion et al., 2007) to obtain images if the sub-seabed structure from ocean-bottom-hydrophone records. At an instrument spacing of 10 km the procedure benefitted from the large water depth of ~5200 m, providing full coverage along most of the profile (Fig. S4). At the western end of the profile, basement is well imaged, while near the eastern end of the line basement was too deep to be clearly imaged. However, it provides a minimum estimate and along with wide-angle reflections from the basement, the basement geometry could be derived.

TOMOGRAPHIC TRAVEL TIME INVERSION OF FRAME-p3

The area off Iberia is affected by ship's traffic, causing sometimes coherent noise is the record sections. However, in general picking of onsets was straight forward and travel times of first arrival P-waves and secondary arriving wide-angle reflections are hand-picked. Picking uncertainties were 20-30 ms for short-offset P-waves (Pg) and reach 40-90 ms for far-offset P-waves (Pn). Secondary wide-angle reflections had larger uncertainties of 60-90 ms. Uncertainties were estimated using a similar method to Zelt and Forsyth (1994), which is based on the noise before and after the pick. For profile FRAME-p3 picking resulted in 460 Ps, 9640 Pg and Pn arrivals and 620 PmP reflected arrivals. Please note that Pg and Pn has been treated as a single phase, but were inverted in two steps, firstly using near offsets of <20 km and secondly adding far offsets of >20 km and inverting near and far-offsets jointly.

The 2-D seismic P-wave velocity structure was derived using a joint reflection and refraction tomography (Korenaga et al., 2000), revealing the sedimentary structure, crustal and mantle structure and the seismic Moho - where present. The procedure used a hybrid ray-tracing scheme, combining the graph method with further refinements utilizing ray bending with the conjugate gradient method. The iterative inversion is regularized using smoothing and damping constraints. A detailed description of this method is given elsewhere (Korenaga et al., 2000).

We used a layer-stripping and hence top-to-bottom approach, first inverting for the shallow structure of the sedimentary section using near-vertical reflections before inverting for the geometry of the basement using near-vertical reflections (where present) and wide-angle reflections from the top basement (see Fig. S2). However, near-vertical reflections occur only right below OBS/H and therefore may lack lateral coverage. The mirror imaging described

above, provides a much more continuous basement geometry and therefore basement was manually adjusted using constraints from the mirror imaging when not constrained by near-vertical reflections. However, while basement geometry is well-imaged in the west, near vertical reflections do not provide a clear basement reflector in the east were sediment thickness is locally >5 km. Here, basement geometry depends solely on wide-angle reflections are thus its geometry may represent a long-wavelength representation of the top of igneous crust. Thereafter, we inverted for the velocity structure of the basement. We (i) used near offset refracted arrivals, (ii) added the PmP arrivals (using a weighting factor of 1, i.e., depth and velocity kernels are weighted equally) and (iii) inverted for all refracted arrivals and PmP, but keeping the geometry of the Moho basically constant (using a weighting factor of 0.1).

Picking errors and starting velocity models may control inversion results. We therefore chose a nonlinear Monte Carlo-type error analysis to derive model uncertainties of crustal structure (Figs S5 and S6). The approach consists of randomly perturbing the velocity values of the initial model and depth of the Moho reflector to create a set of 100 2-D reference models. In addition, noisy travel time data sets are considered. However, travel times had to remain in the initial time window set by the picking uncertainty and did not vary randomly, but smoothly as expected for seismic refraction branches, in contrast to local earthquake tomography where random errors of individual onsets might be appropriate. We inverted randomly selected pairs of perturbed reference models and travel time data sets. The mean deviation of all the solutions is then taken as a measure of the model uncertainty (Tarantola, 1987). For further details see Prada et al. (2014) using a similar procedure. The approach provided models showing a χ^2 of ~1 and a rms misfit of 58-62 ms for the "crustal" model (Pg + PmP) and 68-73 ms for the inversion of "crust" and upper most mantle model (Pg, Pn + PmP). In general, the models are well resolved with velocity uncertainties of <0.2 s. Please note that the somewhat larger uncertainty at the base of crust of the second case arises from

the fact that small uncertainties in Moho depth are mapped into the lowermost crust by averaging the velocity models and hence causing a small increase in rms misfit (Fig. S6). The ray coverage of the models is represented by the derivative weight sum (DWS), which is a measure of the linear sensitivity of the inversion.

Phase	No. of observations	Rms misfit	Chi-square χ^2
Pg	6792	0.065-0.07	1.15-1.3
Pg + PmP	7357	0.065-0.068	1.05-1.1
Pg + Pn + PmP	10.951	0.062-0.071	<1

Tab. S1. Table with misfit between arrival time picks at all OBS/Hs along FRAME-p3

Further, we used the seismic velocities to yield density from the seismic model. Note, seismic velocity structure for the crust was simplified, introducing a small number of layers with constant density for upper and lower crust as well the upper mantle (Fig. S7). A constant mantle density has been used for the upper mantle. The boundary of velocity derived "crustal" density and constant upper mantel density is either defined by the Moho reflector (solid line in Fig. S7) or a smooth interface marking the crust-mantle transition roughly below the area insonified by seismic rays (broken line in Fig. S7). Its geometry is slightly adjusted to nurture a better fit to the data. However, its depth is kept roughly at the same depth where Moho has been observed in the western oceanic crustal domain. Please note that the gravity field data (Sandwell et al., 2014) support the seismic model. A striking feature is that all major changes in density occur below 5 km (seafloor) and above 13-14 km depth and hence the upper mantle may not contain large amounts of frozen melts. Further, the gravity model did not require to

include any regional features – like thick continental crust just eastward of FRAME-p3, suggesting that the transition to thick continental crust has no major impact on the gravity field along the profile or occurs farther east.

TOMOGRAPHIC TRAVEL TIME INVERSION OF IAM9

Travel time data were kindly provided by Tim Minshull (University of Southampton, UK) from seismic profile IAM-9 (Minshull et al., 2014). Here, we inverted the travel time data applying the same strategy outlined above. Using the very same procedure allows us to compare results from both approaches. With respect to data fit, the original model provided a rms misfit of ~0.1 s, while the tomographic inversions reached improved misfit values of 0.055 to 0.072 s. With respect to the Minshull et al. (2014) model, a major difference is that the westward limit of the serpentinized mantle is shifted approx. 20-30 km westward (Fig. S8). Further, to assess the model uncertainty, we used a Monte Carlo inversion. Note that the structure of the sediments was kept as reported by Minshull et al. (2014). Thus, changes in the Monte Carlo inversion and therefore deviations from the starting model only occurred were refracted arrivals sampled the lowermost sediments. In general, IAM-9 is well resolved with the largest uncertainties occurring were there is a gap of 60 km between OBS in the vicinity of the J-anomaly. Fig. S10 has the interpretation of IAM-9 as used for FRAME-p3 (see Fig. 2). In Fig. S11 we show velocity depth profiles for IAM-9 as well as for WE1 of Davy et al. (2016). Features are discussed in the main manuscript.

ACKNOWLEDGEMENTS

MN acknowledges support from FCT (Portuguese Science Foundation) through LISA project (PTDC/CTA-GEF/1666/2020). Institut de Ciències del Mar and MP benefitted from support

of the ‘Severo Ochoa Centre of Excellence’ accreditation of the Spanish “Ministerio de Ciencia, Innovación y Universidades” 2020-2023 (CEX2019-000928-S).

CITED REFERENCES

Davy, R. G., Minshull, T. A., Bayrakci, G., Bull, J. M., Klaeschen, D., Papenberg, C., Reston, T. J., Sawyer, D. S., and Zelt, C. A., 2016, 2016, Continental hyperextension, mantle exhumation, and thin oceanic crust at the continent-ocean transition, West Iberia: New insights from wideangle seismic, J. Geophys. Res. Solid Earth, v. 121, 3177–3199, doi:10.1002/2016JB012825.

Grion,S., Exley, R., Manin, M., Miao, X.-G., Pica, A., Wang, Y., Granger, P. Y., and Ronen, S., 2007, Mirror imaging of OBS data, First Break, v. 25, 37-42.

Grevemeyer, I., Ranero, C. R., and Ivandic, 2018, Structure of oceanic crust and serpentinization at deep-sea trenches, Special themed issue "Subduction top to bottom 2" edited by G.E. Bebout et al., Geosphere, v. 4(2), 395–418, doi:10.1130/GES01537.1.

Korenaga, J., Holbrook, W. S., Kent, G. M., Kelemen, P. B., Detrick, R. S., Larsen, H.-C., Hopper, J. R., and Dahl-Jensen, T., 2000, Crustal structure of the southeast Greenland margin from joint refraction and reflection seismic tomography, J. Geophys. Res., v. 105, 21,591–21,614.

Minshull, T. A., Dean, S. M., and Whitmarsh, R. B., 2014, The peridotite ridge province in the southern Iberia Abyssal Plain: Seismic constraints revisited, J. Geophys. Res. Solid Earth, v. 119, 1580–1598, doi:10.1002/2014JB011011.

Prada, M., Sallares, V., Ranero, C. R., Vendrell, M. G., Grevemeyer, I., Zitellini, N., and de Franco, R., 2014, Seismic structure of the Central Tyrrhenian basin: Geophysical constraints on the nature of the main crustal domains, J. Geophys. Res. Solid Earth, 119, v. 52–70, doi:10.1002/2013JB010527.

Sandwell, D. T., Müller, R. D., Smith, W. H. F., Garcia, E., and Francis, R., 2014, New global marine gravity model from CyoSat-2 and Jason-1 reveals buried tectonic structure. Science v. 346, 65-67, doi:10.1126/science.1258213.

Tarantola, A., 1987, Inverse Problem Theory: Methods for Data Fitting and Model Parameter Estimation, pp. 613, Elsevier Science, New York.

Thébault E., Finlay C.C., Beggan C.D., et al. 2015, International Geomagnetic Reference Field: the 12th generation. Earth, Planets, Space, v. 67, 79, doi:10.1186/s40623-015-0228-9

Verhoef, J., Roest, W. R., Macnab, R., and Arkani-Hamed, J., 1996, Magnetic anomalies of the Arctic and North Atlantic Oceans and adjacent land areas, Open File 3125 of the Geological Survey of Canada.

Zelt, C. A., and Forsyth, D. A., 1994, Modeling wide-angle seismic data for crustal structure: Southeastern Grenville Province, J. Geophys. Res., v. 99, 11687–11704, doi:10.1029/93JB02764

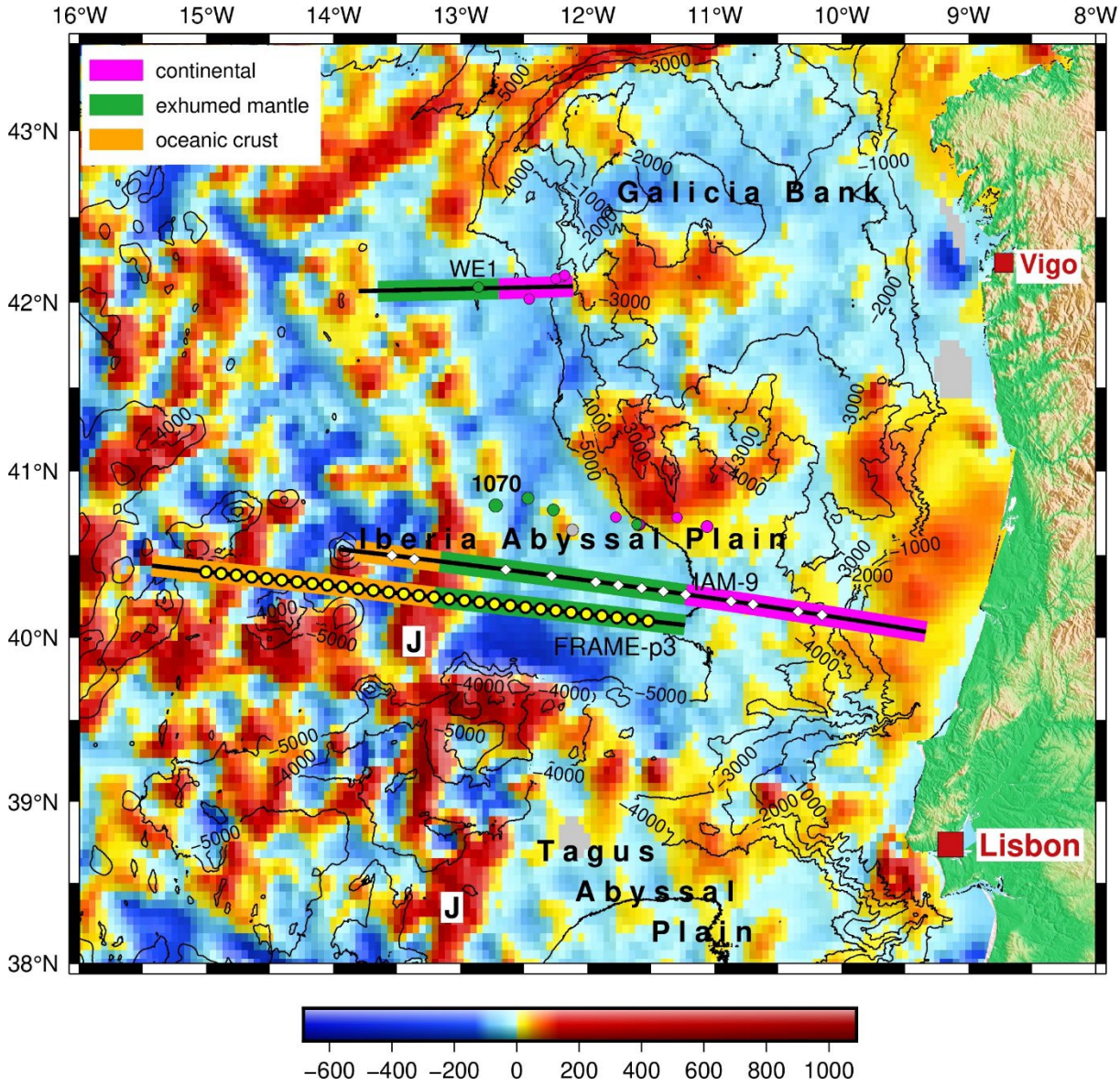

Fig. S1. Magnetic field of the West Iberia margin (Verhoef et al., 1996). Otherwise as Fig. 1.

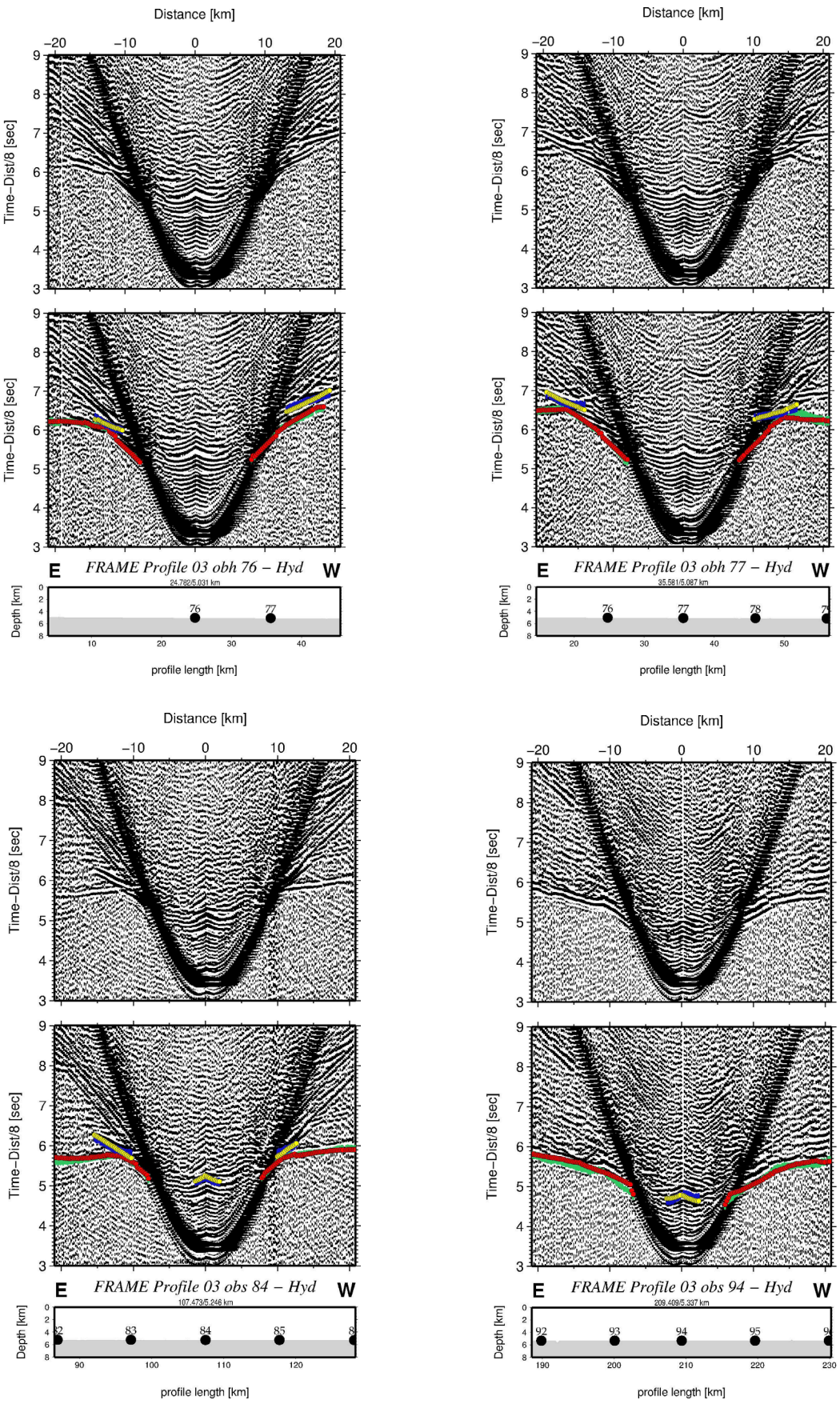

Fig. S2. (top left) OBH76, (top right) OBH77, (bottom left) OBS84, (bottom right) OBS94. Observed reflected arrivals in blue, refracted arrivals in green. Calculated onsets of basement reflection in yellow and refracted arrivals in red.

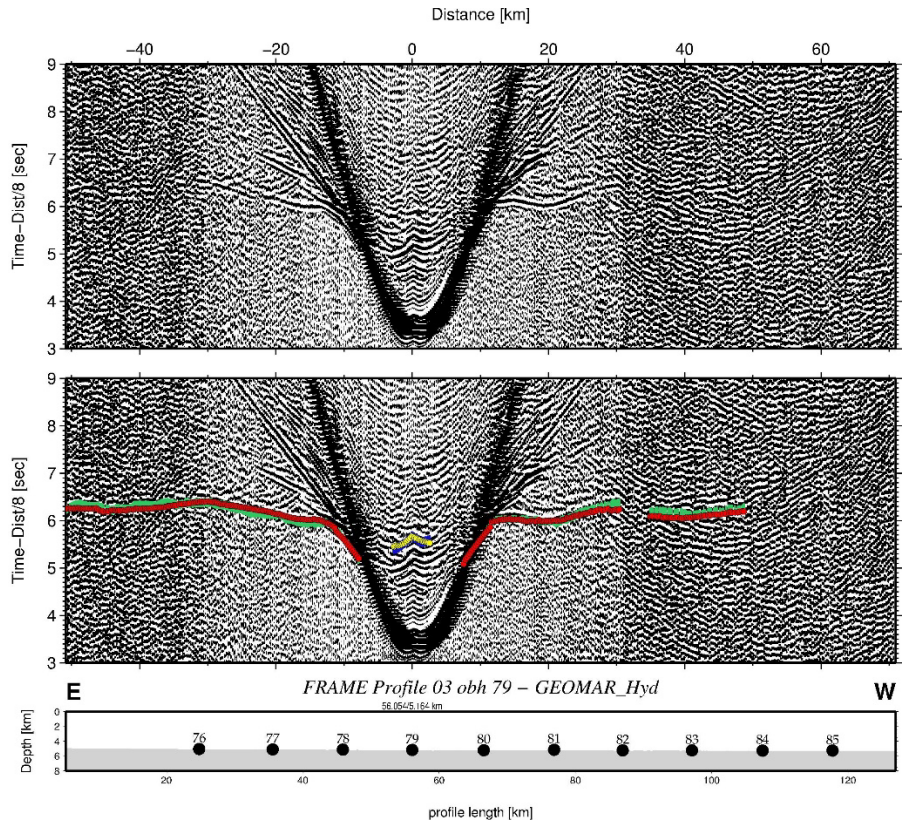

Fig. S3a. Record section of OBH79. Observed arrivals in blue (basement reflection) and turning energy in green. Observed in yellow and red, respectively.

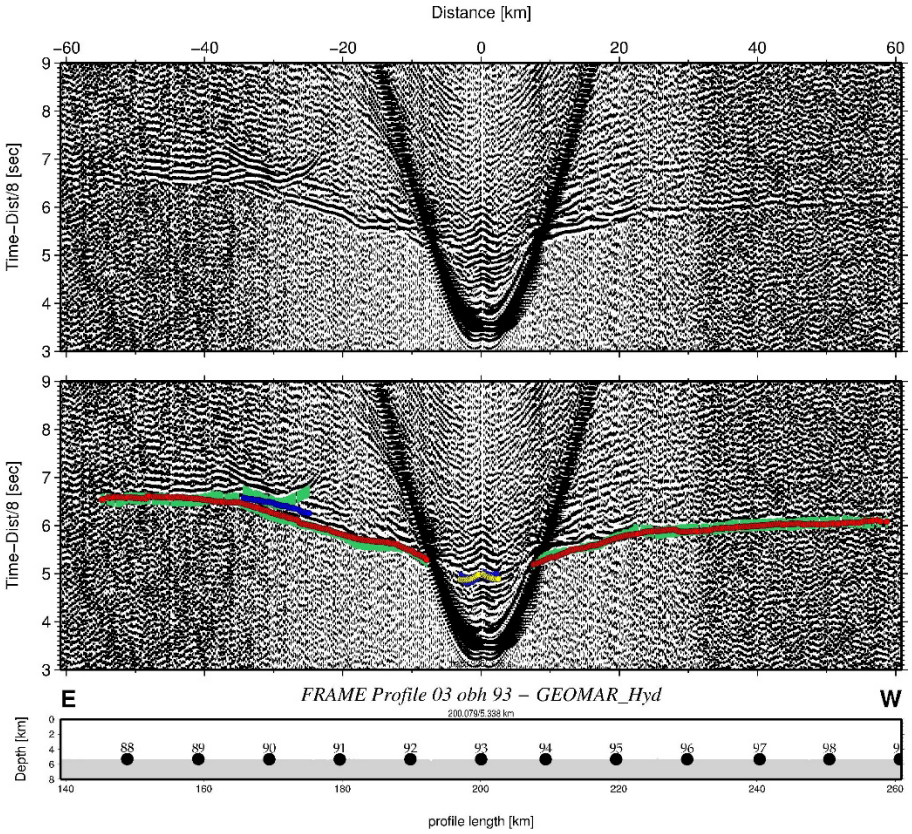

Fig. S3b. Record section of OBH93, otherwise as Fig. DR3a; Blue dots are PmP arrivals.

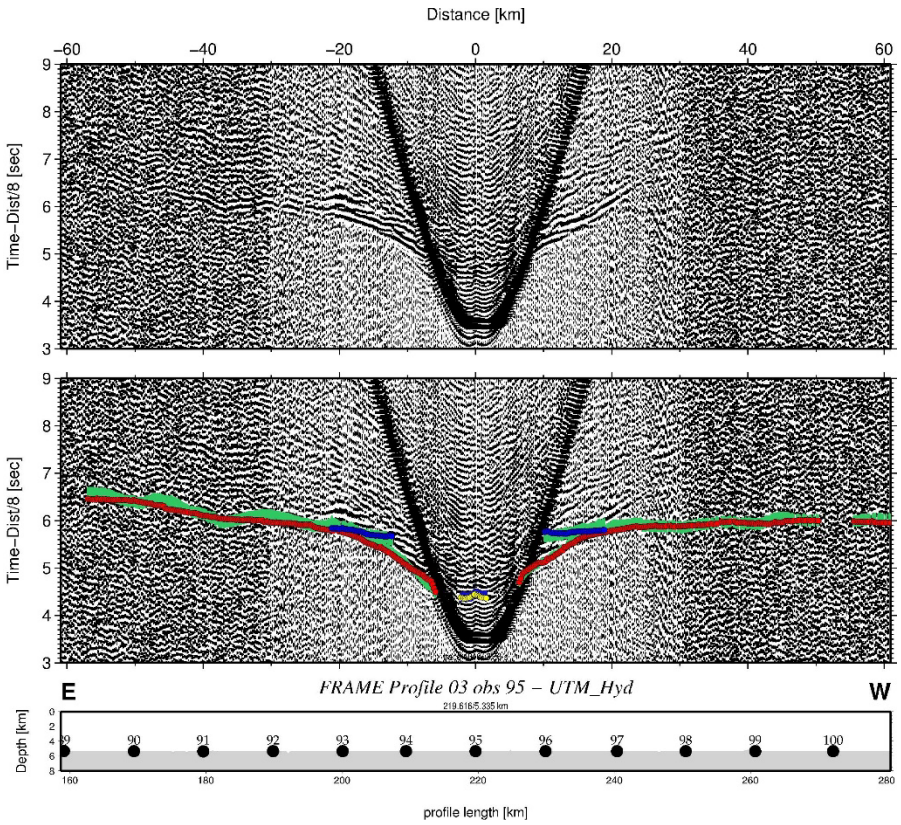

Fig. S3c. Record section of OBS95, otherwise as Fig. DR3b.

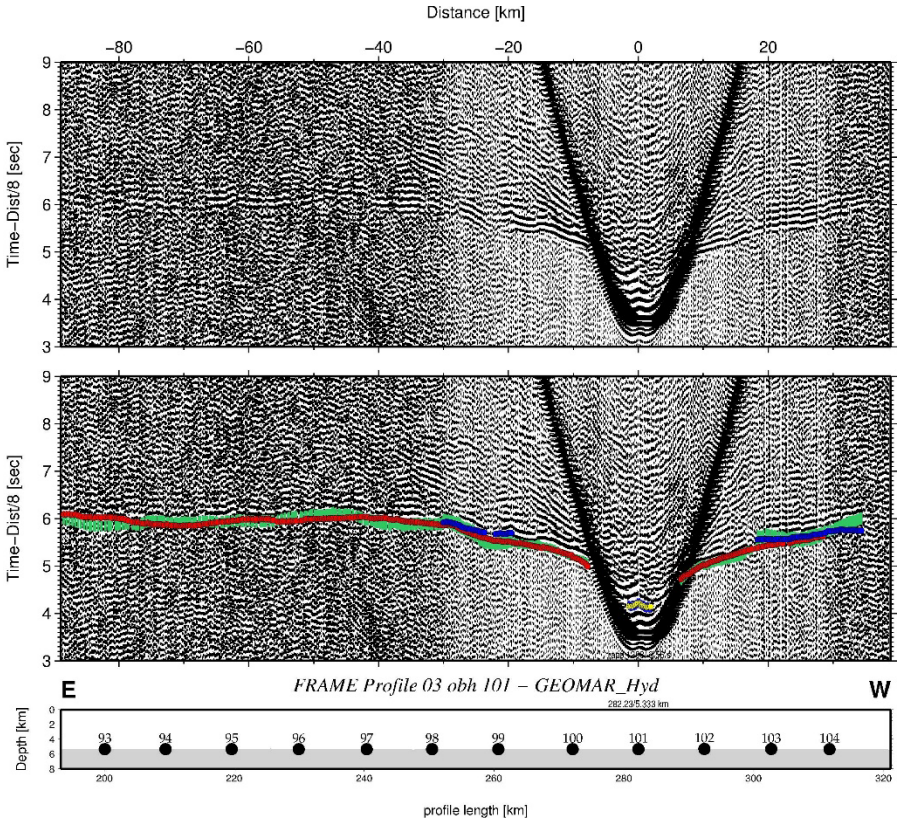

Fig. S3d. Record section of OBH101, otherwise as Fig. DR3b.

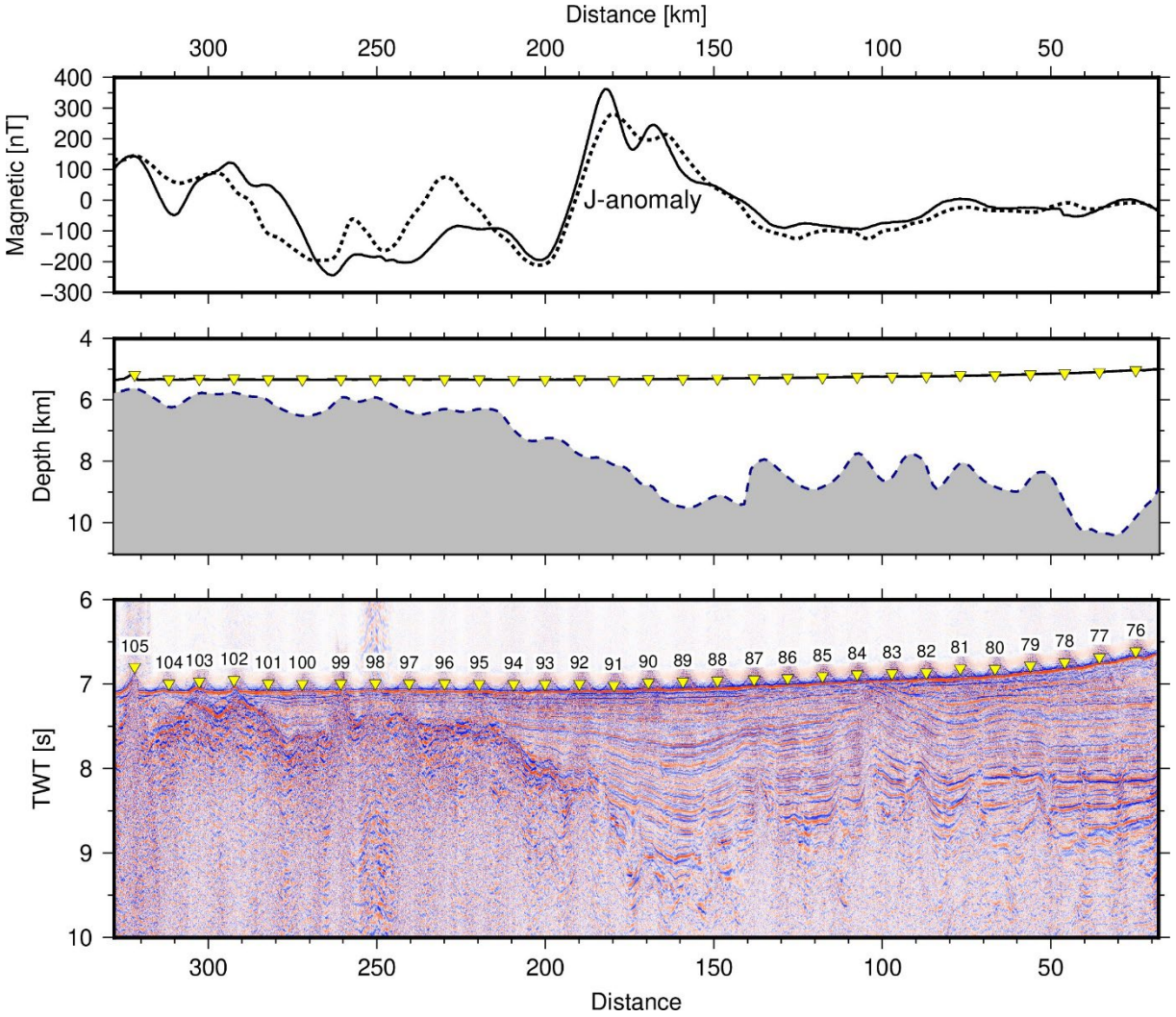

Fig. S4. (bottom) Mirror image of FRAME-p3 and (middle) basement depth inferred from seismic data. (top) Broken line is the magnetic field along the profile extracted from gridded data (Verhoef et al., 1996) and the solid line are the shipboard data corrected for daily variations.

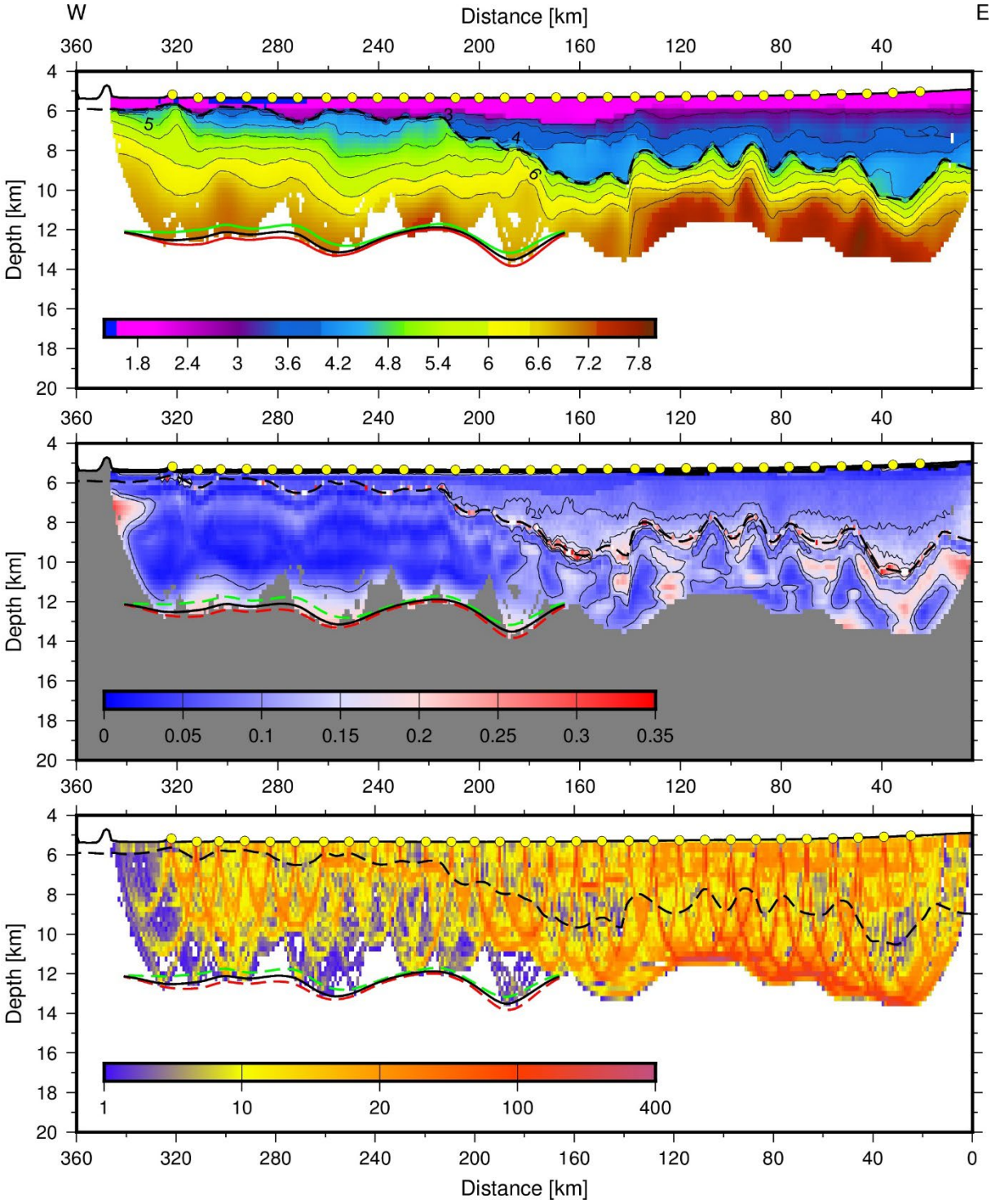

Fig. S5. Results from Monte Carlo Inversion for FRAME-p3 using "crustal" arrivals and Moho reflections. (top) average velocity model with velocity in km/s, (middle) rms misfit in seconds, (bottom) derivative weight sum or weighted ray coverage. Broken line is the basement.

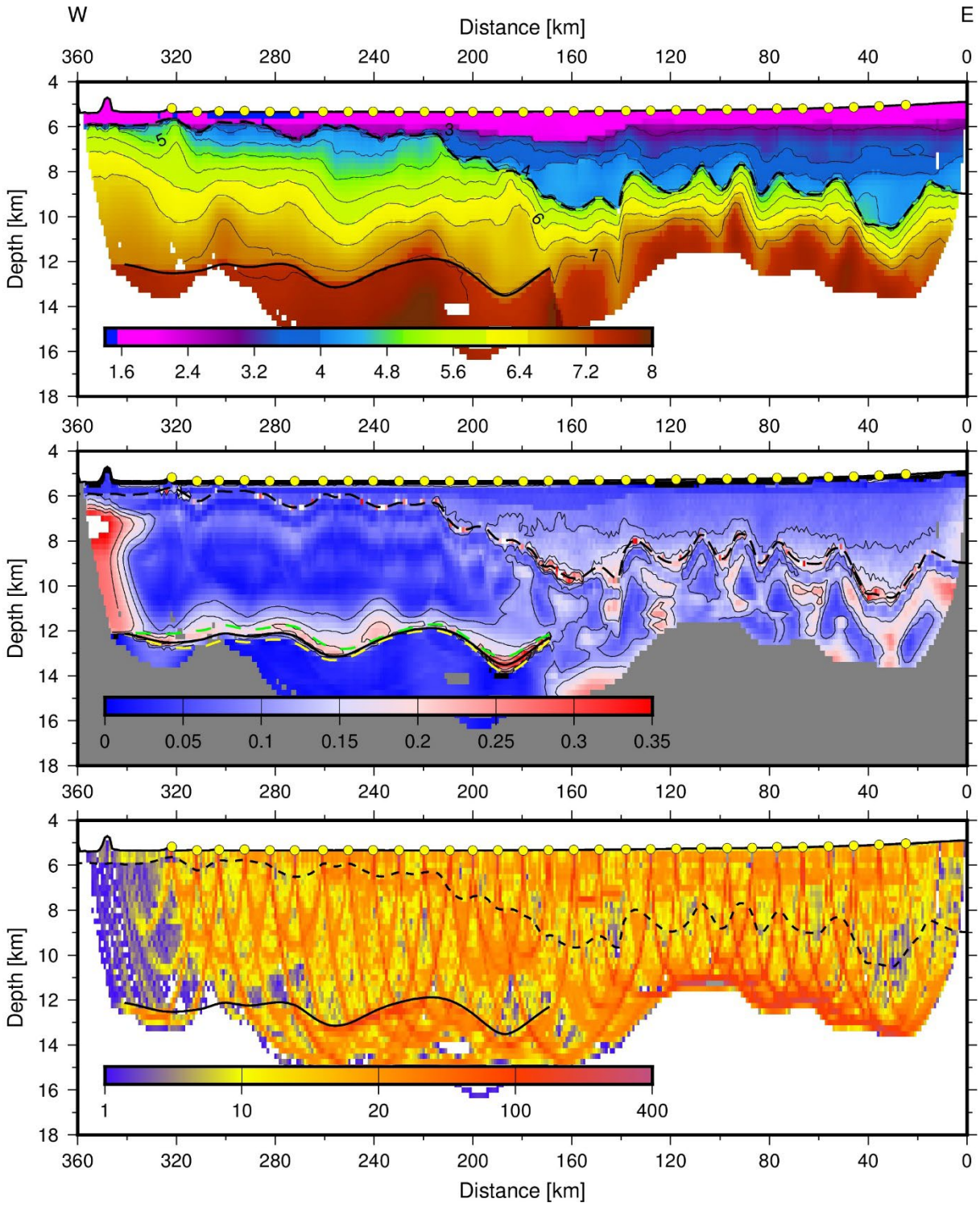

Fig. S6. Results from Monte Carlo Inversion for FRAME-p3 with all refracted arrivals and wide-angle Moho reflections. Otherwise as Fig, S5.

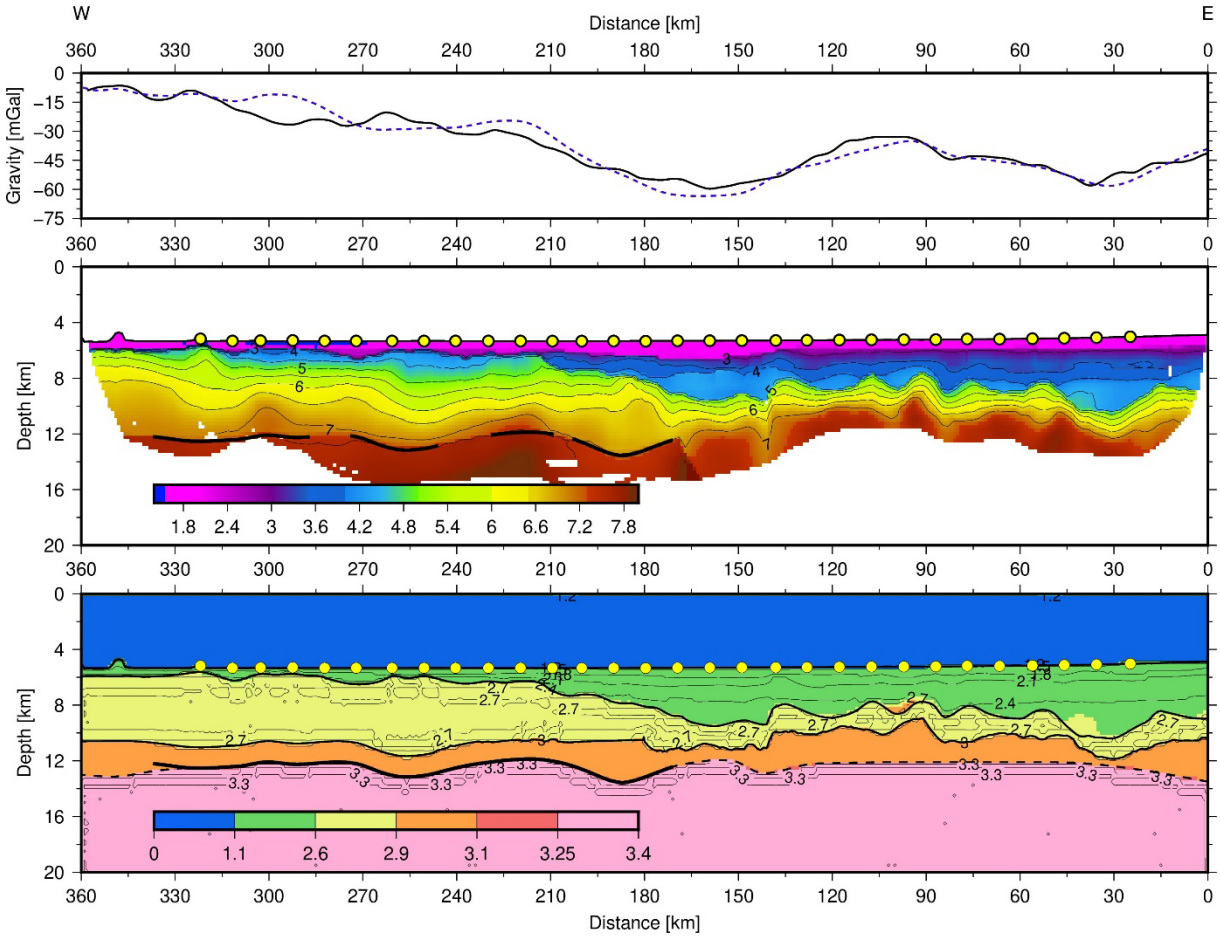

Fig. S7. Calculated gravity field for FRAME-p3. Black line: observed field (Sandwell et al., 2014), broken blue line: calculated field; middle: seismic velocity structure; bottom: density structure (density isolines are shown at a contour interval of 0.3 g/cm3).

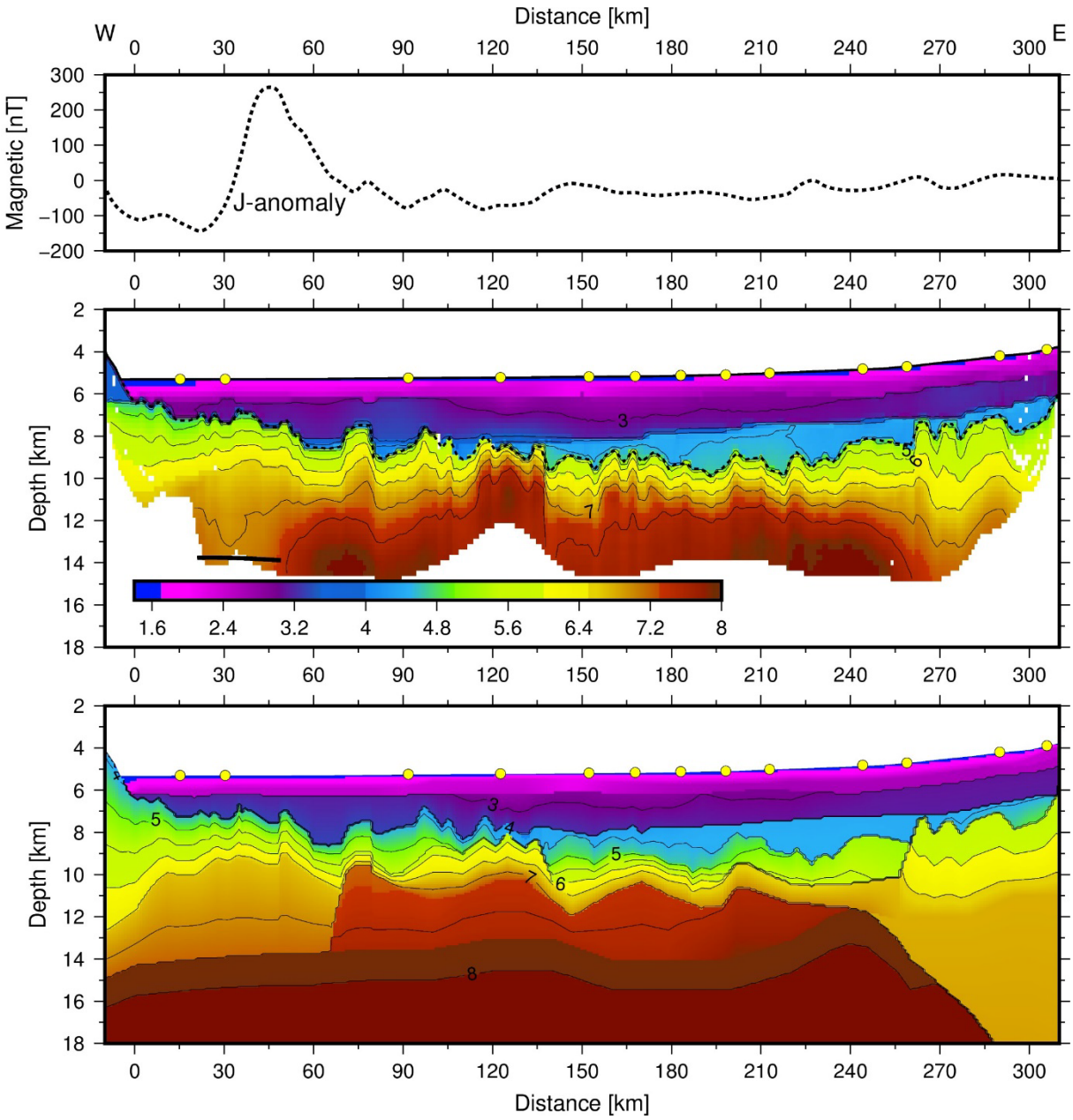

Fig. S8. (top) magnetic field along IAM9 (Verhoef et al., 1996), (middle) new tomographic model, (bottom) forward model of Minshull et al. (2014).

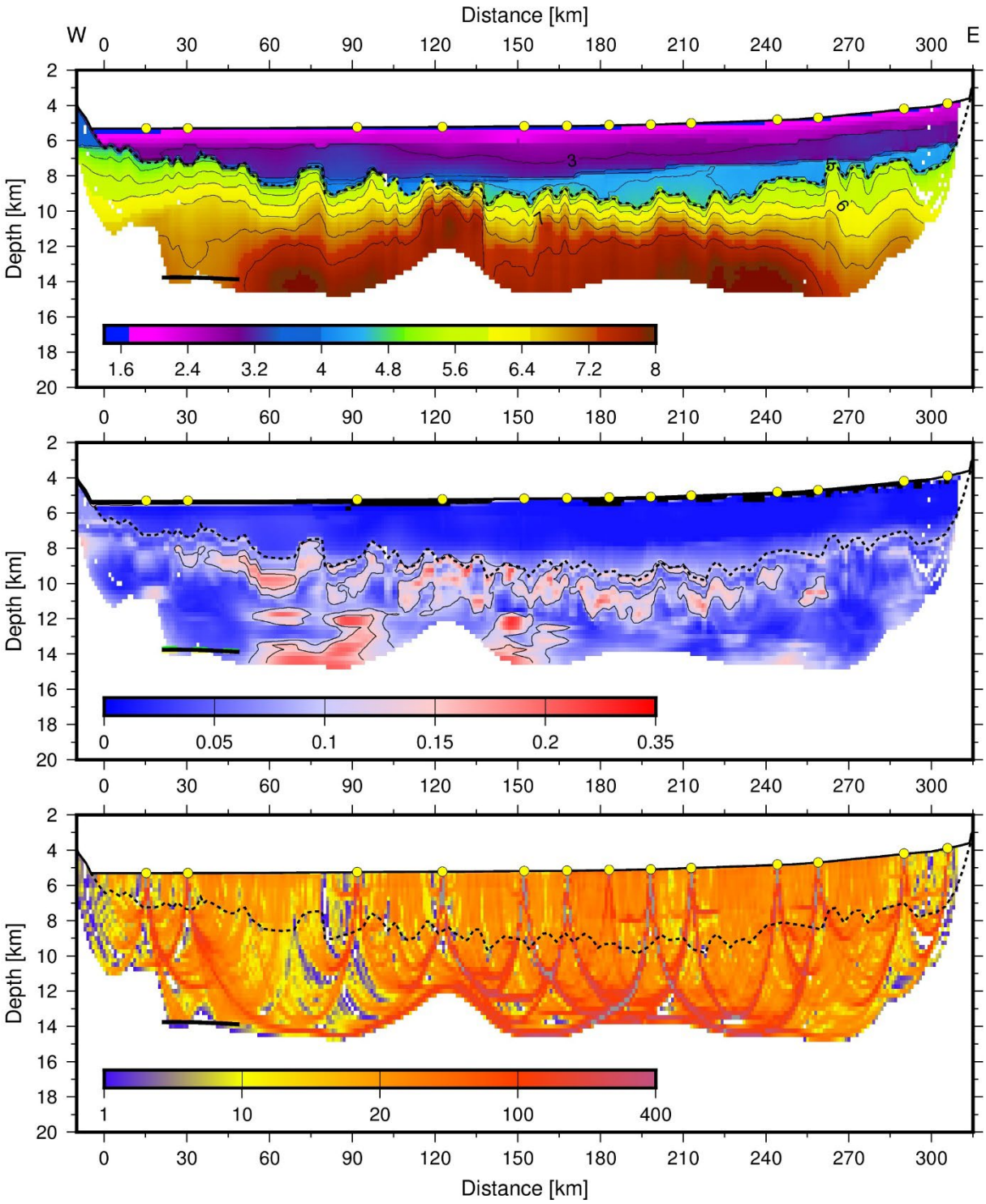

Fig. S9. Results from Monte Carlo Inversion for IAM9 with all refracted arrivals and wide-angle Moho reflections. Otherwise as Fig, DR5.

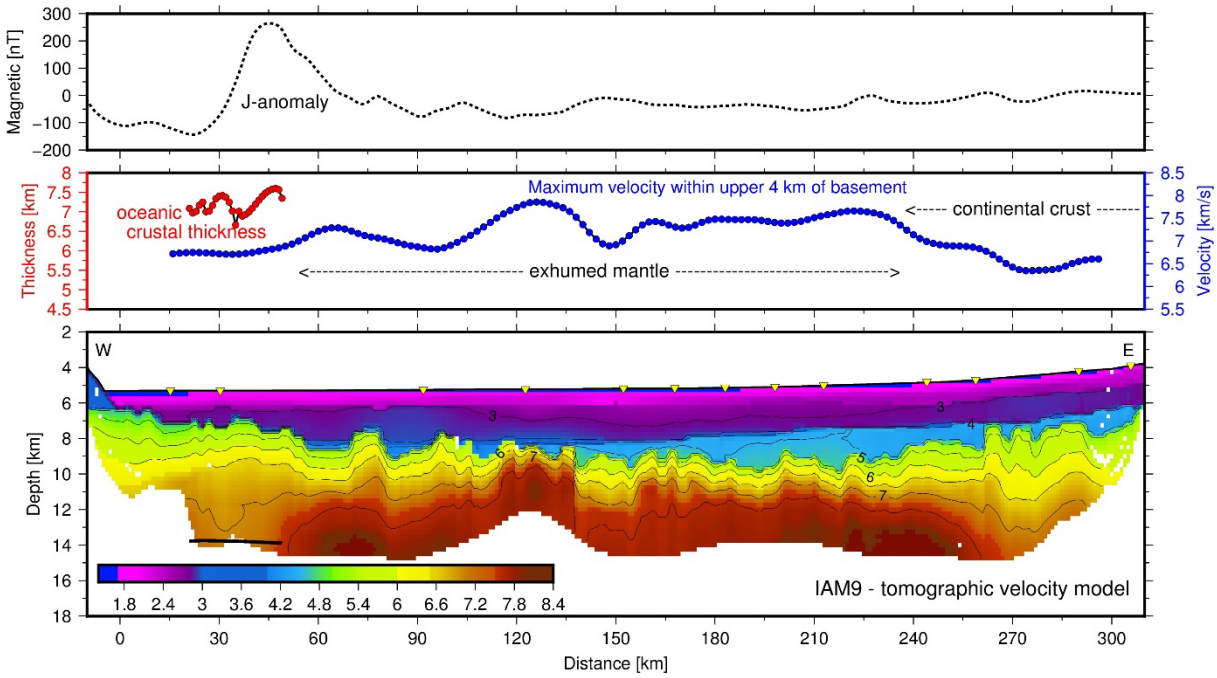

Fig. S10. Results from IAM9 using the same criteria as used form FRAME-p3 in Fig. 2.

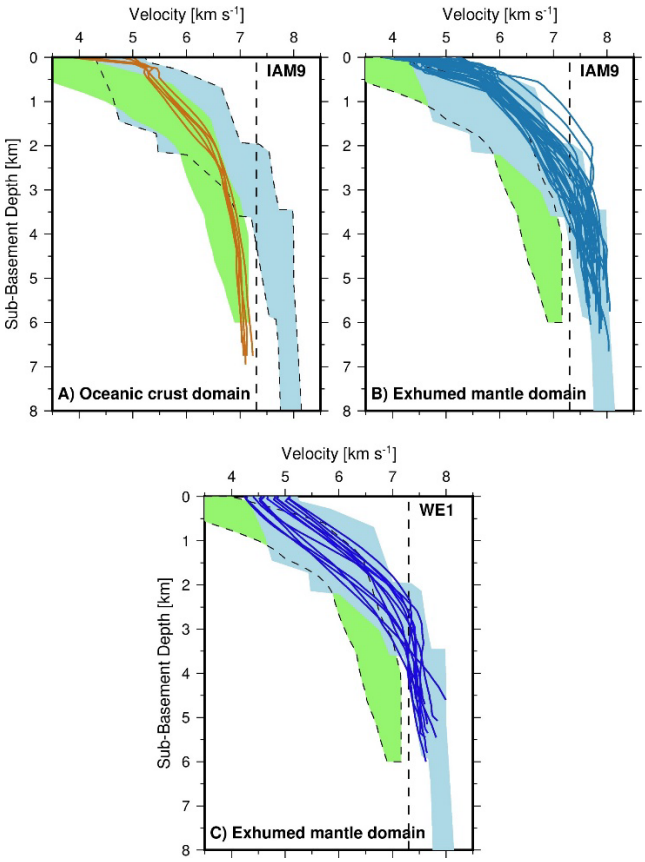

Fig. S11: Classification of the structure along IAM-9 based on velocity depth profiles taken every 5 km. A) crust formed by seafloor spreading; green field: oceanic crust found at segment ends of the Mid-Atlantic Ridge (Grevemeyer et al., 2018), blue field: serpentinized

mantle (Prada et al., 2014), red: onset of seafloor spreading (km 25 to 45); B) exhumed mantle (km 50 to 220); fields as in A; C) exhumed mantle along WE1 (Davy et al., 2016), please note, WE1 does not show any velocity structure resembling normal oceanic crust as found along FRAME-p3 and IAM-9, but may have locally a thin carapace of basalts (< 1 km) on top of hydrated mantle (Davy et al., 2016); fields as in A.